Editors' Suggestion

Ripplocations: A universal deformation mechanism in layered solids

M. W. Barsoum,[1,*] X. Zhao,[2] S. Shanazarov,[1] A. Romanchuk,[1] S. Koumlis,[2] S. J. Pagano,[2] L. Lamberson,[2,†] and G. J. Tucker[3,‡]

[1]*Department of Materials Science and Engineering, Drexel University, Philadelphia, Pennsylvania 19104, USA*
[2]*Department of Mechanical Engineering, Drexel University, Philadelphia, Pennsylvania 19104, USA*
[3]*Department of Mechanical Engineering, Colorado School of Mines, Golden, Colorado 80401, USA*

(Received 19 July 2018; published 2 January 2019)

Layered solids are ubiquitous in nature: from subnanometer graphene and mica layers, to wood, laminated composites, and paperboard at the centimeter scale, to geologic formations at the kilometer range. And while the similarities between the latter two have been recognized [Budd *et al.*, Philos. Trans. R. Soc. A **370**, 1723 (2012)], what has not is that the same physics applies at the atomic-layer scale of crystalline solids. Herein, using a combination of atomistic simulations of graphite and simple instrumented cylindrical indentation experiments on various layered solids—plastic cards, thin steel, and Al sheets—we show that in *all* cases, confined buckling results in an instability that leads to the nucleation of multiple, oppositely signed ripplocation boundaries that rapidly propagate away from under the indenter in a wavelike manner. Crucially, upon unloading, they disappear, after dissipating considerable amounts of frictional energy. Understanding ripplocation nucleation, self-assembly, and propagation is fundamental to understanding the deformation of *most* layered solids.

DOI: 10.1103/PhysRevMaterials.3.013602

I. INTRODUCTION

Layered solids—defined herein as solids in which the deformation, at least initially, is confined to two dimensions—are ubiquitous in nature and span more than 13 orders of magnitude in scale: from subnanometer graphene layers, to wood, laminated composites, and paperboard, at the centimeter scale, to geologic formations at the 100 km, or greater, range. And while historically these very different systems have been studied by their respective communities with little crosstalk, more recently their commonalities have been appreciated (see Ref. [1] and papers therein). In these systems, buckling, delaminations, and nonlinearities are common themes.

In layered crystalline solids, such as graphite, mica, and the MAX phases [2] (layered transition-metal ternary carbides and nitrides), among many others, basal dislocations (BDs) have long been assumed to be the operational micromechanism in their deformation [3–10]. In all other domains [1]—geology [11,12], layered composites [13–15], wood [16], laminated paperboard [17], and rubber layers [18,19]—BDs are not invoked. Instead it has also long been appreciated that a buckling mechanism—that typically results in kink bands comprised of two, or more, kink boundaries (KBs)—occurs. It follows that the fact that many crystalline layered solids fail in compression, but *not* tension, by forming KBs, which are quite similar to those seen in other fields, should have been the first clue that perhaps invoking BDs—as some of us [8] and others [3–10] have done—may not have been the most fruitful avenue. Said otherwise, failure of layered solids is agnostic as to whether the layers are crystalline or amorphous. This observation alone, together with the sharpness of Occam's razor, suggest that BDs, whose existence requires crystallinity, are not involved. BDs were, however, until quite recently, "the only game in town."

Another serious disconnect has been the one between researchers studying crystalline layered geologic solids such as micas, where it was assumed that BDs are the operative micromechanism, and those working on geologic formations that totally ignore the microscopic aspects. If BDs are important at the microstructural level, should they not also feature in the "big picture"? This work attempts to address some of these discrepancies and paradoxes.

Recently, we argued that layered crystalline solids do not deform by BDs, as commonly assumed [20–22], but rather via the nucleation and propagation of ripplocations—a term coined in 2015 by Kushima *et al.* [23] to explain near-surface deformations in van der Waals solids. In 2016, using a combination of molecular dynamics (MD) on graphite at 10 K and transmission electron microscopy (TEM) observations on Ti_3SiC_2—a MAX phase—we made the case that ripplocations were a new micromechanism in the deformation of layered solids. In 2017, we presented nanoindentation and TEM results obtained on Ti_3SiC_2 and argued that they only made sense in a ripplocations framework [20]. Quite recently, we also studied the nucleation of ripplocations in graphite and defined ripplocation boundaries (RBs) to be boundaries that are fully and spontaneously reversible. We also showed that these RBs—that nucleate by the alignment of ripplocations on adjacent layers—are exceedingly nonlocal, and propagate, wavelike, away from the indented surface [22]. RBs feature prominently in this work.

Since BDs cannot result in *c*-axis strain, clear evidence for the latter rules them out [20,24]. The dilemma is best seen in

*Corresponding author: barsoumw@drexel.edu
†Corresponding author: lel59@drexel.edu
‡Corresponding author: tucker@mines.edu

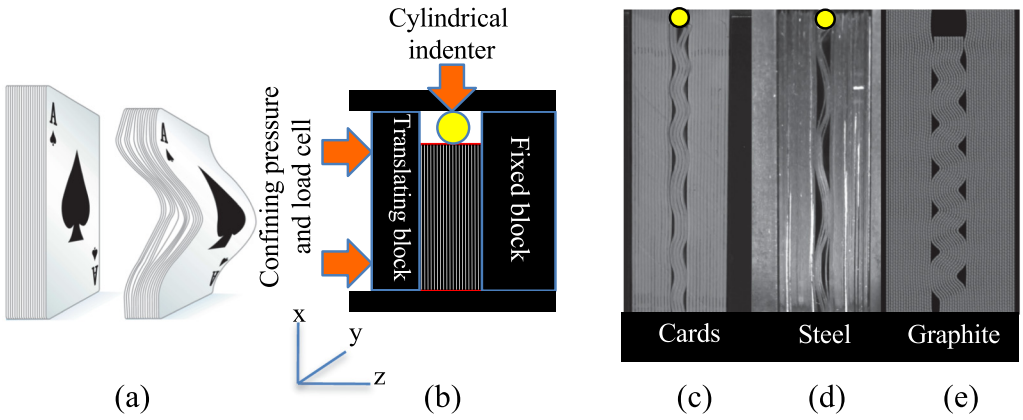

FIG. 1. (a) Kinking of a deck of unconstrained cards loaded edge-on in compression. (b) Experimental setup used. Snapshots of ripplocations formed when a cylindrical indenter is loaded edge-on into (c) plastic cards, (d) steel plates, and (e) graphite. The latter is a result of a MD simulation.

Fig. 1(a); that the cards can slide relative to each other is not a stretch. In a typical layered, hexagonal crystalline solid, such sliding would be mediated by BDs. Such slip, however, *cannot* account for the all-important c-axis strain that is observed. Said otherwise, while BDs can explain the relative sliding of the layers, they cannot explain what actually happens wherein cards move normal to their planes. The leitmotiv of this paper is that for the all-important motion normal to the layers to occur, the cards have to *buckle*.

Before proceeding further, another characteristic of layered solids that, until recently, has resisted a correct interpretation is the response of kinking nonlinear elastic (KNE) solids to compression [8,25–28]. KNE solids are characterized by stress-strain curves that are fully and spontaneously reversible—not unlike the ones shown in Figs. 4(a)–4(c)—and during which considerable energy can be dissipated per cycle. Such behavior has been observed in the MAX phases [28], mica [29], and graphite [30], among many other layered solids.

The purpose of this work is to present direct macroscopic evidence for ripplocations. Our results also finally explain the origin of the aforementioned energy dissipation and full reversibility observed in KNE solids. To that effect, we loaded—edge-on with a cylindrical indenter [Fig. 1(b)]—and filmed a deck of plastic playing cards, thin aluminum, Al, and steel sheets. Both the loads on the indenter, P, and those normal to the layers, P_N [viz., along z in Fig. 1(b)], were measured as a function of penetration of the indenter, h, into the layers. Figures 1(c) and 1(d), respectively, show the configurations obtained when the thin steel sheets and cards were loaded. Figure 1(e) shows the results of a molecular dynamics (MD) simulation when 60 graphite layers are confined and loaded with a 5-nm-diameter cylindrical indenter. The similarity between the three configurations is obvious. What is also undeniable is that for the most part, the wavelengths of the ripplocations, λ, are of the same order as the indenter diameter, δ. In some cases, λ is several times that of the indenter radius [see Fig. 1(d)]. Note that this is only true when the indenter diameter δ is of the same order as the layer thicknesses t. If $\delta \gg t$, the situation is different and quite complex microstructures rapidly evolve [20,21].

II. EXPERIMENTAL AND COMPUTATIONAL DETAILS

A. Mechanical tests

Figure 1(b) shows a schematic of the setup used in which a set of layers is loaded edge-on with a 2.00 mm or 2.34-mm-diameter cylindrical indenter, with its axis parallel to the layers to be indented [the chosen coordinate axes are shown at the bottom left of Fig. 1(b)]. The layers to be loaded are placed between a fixed and a translating block that is equipped with a load cell that measures the initial confining load, $P_{N,0}$, as well as the load that develops, P_N,—along z—as a result of the indenter penetrating into the layers. In a typical experiment, 40 to 60 layers are placed between the fixed and moveable blocks [Fig. 1(b)] and a load, along z, corresponding to a $P_{N,0}$ of 400, 1200, or 2400 N is applied. The indenter is then thrust, from the top, and both the penetration or displacement, d, and load, on the indenter, P, are recorded. Concomitantly, P_N is also recorded. Three different materials were tested: 0.3-mm-thick plastic playing cards, 0.17-mm-thick steel sheets, and 0.17-mm-thick Al sheets. These materials were chosen to cover a wide range of elastic and plastic properties. Furthermore, to explore the effect of friction, a few experiments were conducted on steel sheets that were precoated with a layer of MoS_2.

The indentations were carried out in displacement control mode. Two types of experiments were carried out. In the first, the indenter was thrust into the layers up to a given maximum indentation depth, h_{max}, fully unloaded and reloaded to progressively higher h values (see Fig. S4 in SM [31]). In the second, the indenter was loaded to h_{max}, retracted to a $h < h_{max}$, reloaded to h_{max}, and unloaded to progressively lower h values [see Figs. 4(a) and 4(b)]. All experiments ended with the total retraction of the indenter. More details on the mechanical tests can be found in the Supplemental Material [31]. We also used the inclined plane method to measure the friction between the plastic cards and the steel sheets before and after coating the latter with MoS_2. The results are shown in Table S1. The geometries of the various setups are summarized in Table S2 of the Supplemental Material (SM) [31].

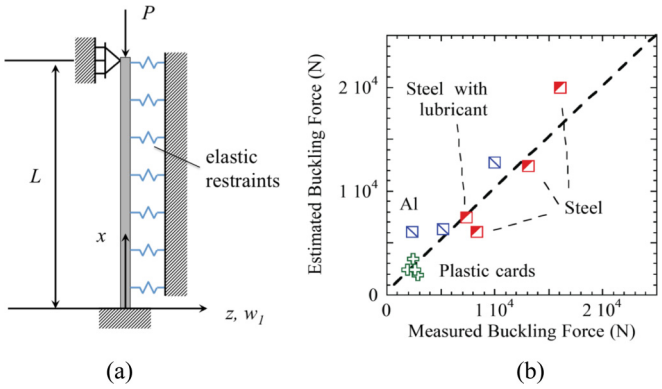

FIG. 2. (a) Schematic of system used to analyze critical buckling load on a confined layer simulating ripplocation formation at the continuum scale. Elastic restraints modeled as springs, along the length, act as the confinement load and neighboring layers. (b) Comparison of measured and calculated [Eq. (2)] buckling loads for the cards, Al, and steel sheets.

B. Buckling analysis

To demonstrate that the behavior of the indenter experiments on confined layers of various materials can be modeled using elastic buckling theory, and is thus instability driven, we present a first-order approximation of the critical buckling loads, P_{Bk}, which lead to ripplocation nucleation. To simplify, a single layer that acts as a Euler column, loaded axially with load, P, with a continuous elastic restraint along its length (Fig. 2) is analyzed. L is the original length of the layers.

The following approach is used to model the indenter load pushing on layers, which feel the resistance laterally due to friction from neighboring layers, and indirectly from the confinement load restraining lateral motion. We consider the loaded material layers to act in a homogeneous manner with a flexural rigidity EI of the base material (e.g., plastic, aluminum, or steel), where E is the Young's modulus and I is the second moment of inertia. Here, I is assumed to be given by

$$I = \tfrac{1}{12}(nt)^3 b,$$

where t is the thickness of a single layer, n is the total number of layers indented, and b is the width of the layers, i.e., along the y direction (Fig. S1 in the SM). Using this expression assumes the n layers are welded together and thus ignores layer parallel shear. This is valid here since the confined layers remain in contact and there is little to no relative slip observed between the layers (as shown by images and movies in the SM [31]). This is especially true just before the nucleation of the ripplocations. The fact that the maxima and minima locations of highest curvature, of the n-buckled layers, are happening in phase also shows that the n layers can be thought to behave, or act, as a single unit, at least for the sake of a first-order approximation of the buckling behavior assumed herein.

The continuous restraints along the length act as the confinement load and neighboring layers, and are modeled by springs of equivalent stiffness c. We assume the latter is the measured confinement force, P_{N}, at experimental critical load, $P_{\mathrm{N,crit}}$, divided by the deflection of the springs (w_l). The latter is the deflection of the layers along z, measured by the image processing software IMAGEJ. For unit consistency with the presented solution, we divide c by the length of the beam to get a stiffness per unit length or $\mathrm{N/m^2}$. In other words,

$$c = \frac{P_{\mathrm{N,crit}}}{L w_l}.$$

The governing buckling equation for this idealized case is given by [32]

$$\frac{d^4 w}{dx^4} + \alpha \frac{d^2 w}{dx^2} + \xi w = 0, \tag{1}$$

where $x = x_i/L$, $w = w_i/L$, $\alpha = PL^2/(EI)$, and $\xi = cL^4/(EI)$.

The general solution of Eq. (1) is

$$w = C_1 \cos(\mathrm{S}x) + C_2 \sin(\mathrm{S}x) + C_3 \cos(\mathrm{T}x) + C_4 \sin(\mathrm{T}x),$$

where

$$S = \sqrt{\frac{\alpha}{2} - \sqrt{\left(\frac{\alpha}{2}\right)^2 - \xi}}$$

and

$$T = \sqrt{\frac{\alpha}{2} + \sqrt{\left(\frac{\alpha}{2}\right)^2 - \xi}}.$$

The smallest critical load for a periodic solution is given by [32]

$$P_{\mathrm{Bk}} = 2\sqrt{cEI}. \tag{2}$$

The Young's moduli E of the Al and steel sheets were assumed to be 69 and 200 GPa, respectively. E of the plastic cards was measured in tension and found to be ≈0.5 GPa. Further, the assumption of linear elasticity made for the analysis may not hold as strongly for the plastic playing cards as for the Al and steel.

C. Computational details

To model the indentation of graphite, we employed molecular dynamics at 10 K and an adaptive intermolecular reactive empirical bond order (AIREBO) interatomic potential [33] to govern atomic interactions using the atomistic simulation software package LAMMPS [34]. The simulated graphite structure is composed of 60 layers and is approximately $50 \times 1 \times 20\ \mathrm{nm^3}$ containing 150 000 atoms. Free surfaces were employed in the x direction, while periodic boundary conditions were employed in the y and z directions. A 1-nm-thick region of atoms at the bottom free surface in the x direction was held fixed during the indentation simulation. The indentation was performed along the negative x direction from the top free surface and followed a sinusoidal path to a maximum depth of 2.5 nm and period of 100 000 time steps. Indentation of a 60-layer graphite system was modeled using a cylindrical repulsive potential acting along the y-direction, on all atoms within 25 Å of the indenter center. The indenter diameter was 5 nm.

To study the influence of confining pressure on the system, various target pressures were applied in the lateral z direction, relative to the indentation, in the x direction. The system was equilibrated under the isothermal-isobaric ensemble to a target normal pressure in the z direction ranging from 0 to 5000 bars. Once the target lateral pressure was achieved

during the equilibration phase, the simulation cell length in that direction was held fixed during the indentation phase of the simulation. Periodic boundary conditions in the z direction were maintained throughout equilibration and indentation in all cases.

III. RESULTS AND DISCUSSION

Movies of indentation into the cards, steel, and Al sheets can be found in Movies S1 to S3, respectively, in the Supplemental Material [31]. From these movies, it is obvious that, in all cases, what is occurring is confined buckling. Crucially, and despite the very different materials tested, these movies are quite similar in that in all cases, the sequence of events is as follows: (i) Upon initial loading, the indenter pushes the layers more or less straight down. (ii) At a critical indentation depth, h_{crit}, a very rapid nucleation of multiple, and oppositely signed, collection of ripplocations—that are not sharp but curved—occurs. To distinguish these from KBs, which are *irreversible*, we label these ripplocation boundaries, RBs [22]. It follows that RBs, that are neither sharp nor irreversible like KBs, are their precursors. RBs have a wavelike quality and quite rapidly propagate to the bottom of the stacked layers. (iii) Increasing h increases the amplitudes, but *not* the wavelengths, of the RBs. (iv) With the notable exception of the Al layers indented to a h of 3 mm (see below), all of the other layers recovered *spontaneously* and almost fully upon retraction of the indenter.

In a typical experiment, the layers are placed edge-on between the fixed and movable blocks in Fig. 1(b) and an initial confining load, $P_{N,0}$, is applied. The indenter is then thrust into the layers while recording P, P_N and the displacement. Still frames, taken from Movie S1 of the SM [31] made when the cards, constrained initially by a $P_{N,0}$ of 400 N, were loaded with an indenter with $\delta = 2$ mm, are shown in Figs. 3(a), 3(b), and 3(c). Figure 3(a) shows the cards just before the nucleation of the RBs; Fig. 3(b) shows the cards 0.5 s later, showing the nucleation of RBs of alternating orientations [depicted by red arrows in Fig. 3(b)], starting at the top. Figures 3(c) and 3(d) show the configuration at $h_{max} = 2.5$ mm for $P_{N,0}$ of 400 and 2400 N, respectively. Note that the RBs penetrate deeper for lower $P_{N,0}$. The story these frames tell is in total accord with points (i) to (iv) made above.

Still frames taken from Movie S2 of the SM [31] made when the steel sheets—constrained by a $P_{N,0}$ of 400 N—were loaded are shown in Fig. S2 of the SM [31]. Despite the vastly different elastic properties of these layers, compared to the cards, the response was qualitatively identical. Here again, RBs (red arrows in Fig. S2b of the SM [31]) nucleate at a P_{crit}. An examination of these still frames, and others (not shown), is also in total accord with points (i) to (iv) made above.

Still frames from the movie made when the Al sheets—constrained by a $P_{N,0}$ of 400 N—were indented, before and just after the RBs (denoted by red arrows), nucleated are shown in Fig. S3a and S3b, respectively, of the SM [31]. Figure S3c is the same as Fig. S3a, but at $h_{max} \approx 2.5$ mm. Figure S3d shows the configuration after total unloading, where it is obvious that the initial configuration was more or less restored [31]. Here again these frames are in total accord with points (i) to (iv) made above. Figure S3e shows the configuration after *total retraction* of the indenter indented to h_{max} of 3 mm shown in Movie S3 of the SM [31]. In this case, the stress at the crests/troughs of the RBs exceeded the yield point of the Al sheets, resulting in plastic deformation as evidenced by the fact that upon the indenter's retraction, the RBs do *not* return to their initial, flat state, but are now replaced by KBs denoted by dashed lines. This is best seen by comparing Figs. S3d and S3e, both taken after total retraction of the indenter from different h_{max} values [31].

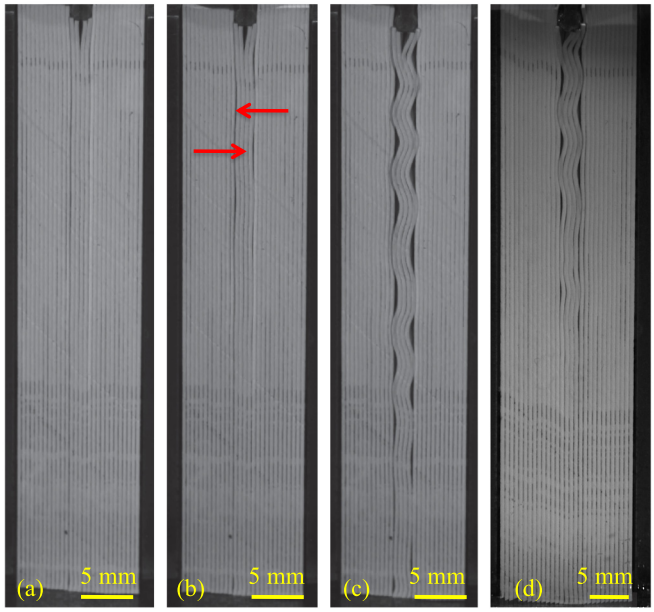

FIG. 3. Still frames from movie (see movie 1 in SM [31]) made when 0.31-mm-thick cards—$P_{N,0} = 400$ N—were loaded with a 2-mm-diameter cylindrical indenter (top): (a) Just before nucleation of RBs, (b) 0.5 s later showing RBs (red arrows) starting at the top, and (c) at h_{max} of 2.5 mm. (d) Same as (c), but for $P_{N,0}$ of 2400 N. Note shallower penetration of ripplocations in (d).

We now turn our attention to the indentation stress-strain (ISS) curves. Figure 4(a) shows the results for the cards. Here three sets of nested curves are shown: The ones depicted by red diamonds, black crosses, and solid blue lines were obtained with $P_{N,0}$ of 400, 1200, and 2400 N, respectively. (The 1200 N results are truncated for clarity's sake.) In all cases, the stress initially increases quasilinearly with strain. At a critical stress, σ_{crit}, denoted by x in Fig. 4(a), the stress more or less levels off. Note that σ_{crit} increases with increasing $P_{N,0}$. When the indenter is partially retracted, the stress follows the trajectory labeled AB in Fig. 4(a). Upon reloading, the stress-strain curves follow the trajectory BA, thus delineating the fully reversible loop ABA. When the process is repeated to lower stresses, a series of nested loops, with a single unloading but different reloading, trajectories are traced. When the same stresses are normalized, as shown in Fig. S5 of the SM [31], the universality of the unloading trajectory is obvious. These ISS curves are qualitatively the same as those that we, and others, have previously observed when loading different MAX and other phases in cyclic uniaxial compression and spherical nanoindentations [8,35,36].

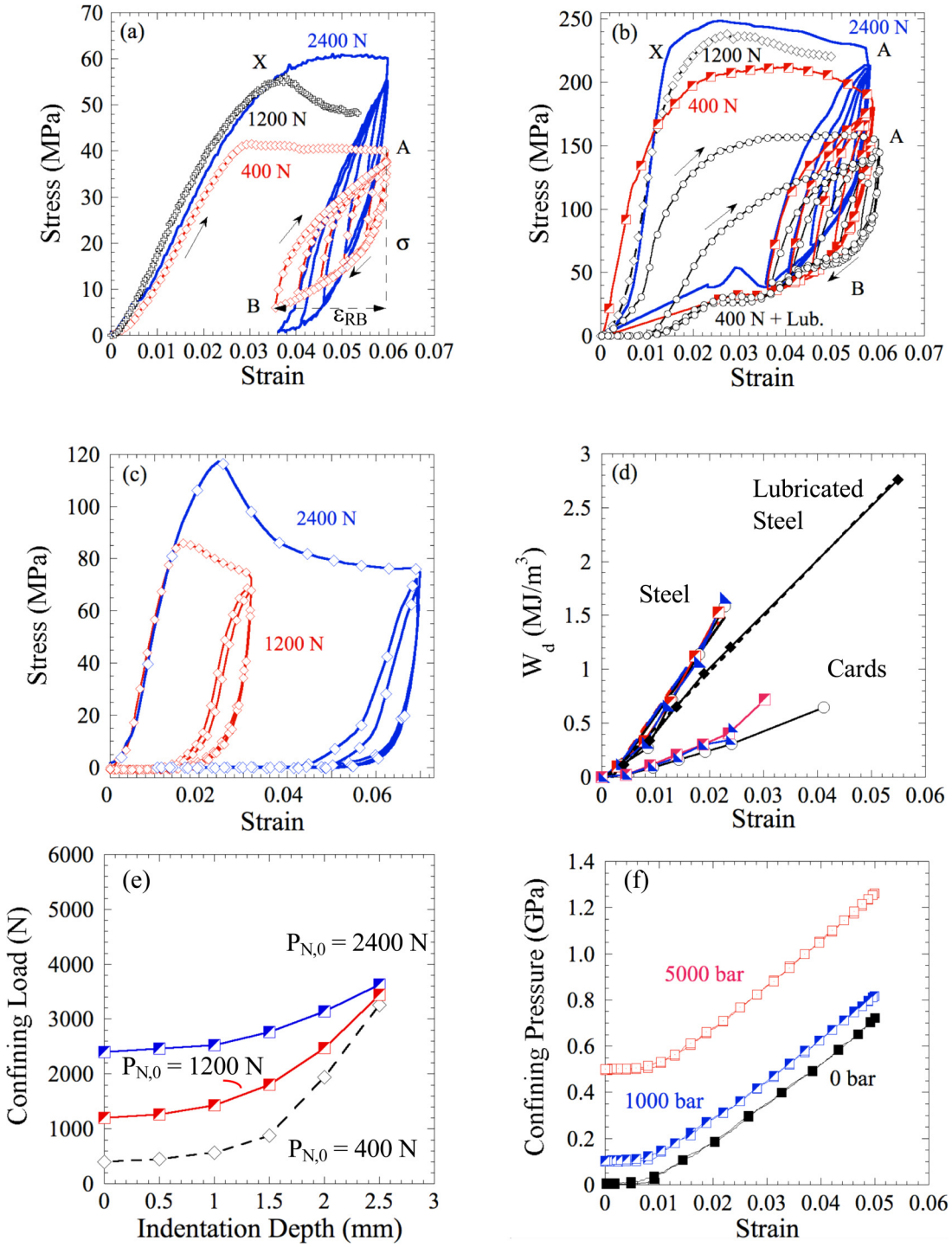

FIG. 4. Mechanical response of indented layers. (a) Indentation stress-strain curves obtained when plastic cards were loaded with a 2.34-mm-diameter cylindrical indenter edge-on for three values of $P_{N,0}$ indicated. (b) Same as (a), but for steel sheets. Loops denoted with open black circles were obtained with $P_{N,0} = 400$ N, after every sheet was coated with a solid lubricant. Arrows show direction of loops. (c) Same as (a), except with Al sheets loaded to two different h_{max} and $P_{N,0}$ indicated. (d) Energy dissipated per unit volume per cycle, W_d vs ripplocation strain. (e) P_N as a function of h for cards. (f) same as (e), but for the MD simulations of graphite layers.

Figure 4(b) plots ISS curves for the steel sheets. Like the cards, the loops depicted by solid blue lines, black open diamonds, and red checkered squares were obtained at $P_{N,0}$ of 2400, 1200, and 400 N, respectively. The loops depicted by black circles were obtained at $P_{N,0} =$ 400 N, but, prior to testing, each steel sheet was brushed with the solid lubricant MoS_2. Two full loading cycles, depicted by arrows, were implemented: the first is the larger in area and the second is enclosed by the first. A permanent strain of ≈0.01 was recorded in the first cycle; the second and subsequent cycles are fully reversible.

Figure S4a of the SM shows the nested loops obtained when the indenter was fully retracted first, and then progressively loaded to larger h values [31]. And while the shapes of these nested loops are qualitatively similar to those shown in Fig. 4(a), they are not as well defined and reproducible as the ones obtained upon partial unloading; viz., Figs. 4(a) or 4(b). The stress-strain curves shown in Figs. 4(a) and 4(b) were therefore used for further analysis.

Figure 4(c) shows the ISS curves obtained when the Al sheets were indented between h_{max} and a fully unloaded state three times when $P_{N,0}$ was 1200 and 2400 N, depicted by red open diamonds and blue diamonds in Fig. 4(c), respectively. For $P_{N,0} = 1200$ N, up to a strain of ≈0.02, the response was, for the second and subsequent cycles, near fully and spontaneously reversible. When h_{max} was increased to 3 mm [blue diamonds in Fig. 4(c)], however, the loops were no longer fully reversible on account of the layer's plastic deformation, as shown in Fig. S3e of the SM [31].

When P_N vs h is plotted for the cards [Fig. 4(e)], in all cases, P_N first increases slowly and then more rapidly with increasing h. At h_{max}, the three curves converge to P_N values between 3200 and 4000 N. To understand these observations, it is imperative to understand the nature of the fully reversible loops (see below).

The results of our elastic buckling analysis are presented in Table S2 of the SM [31], in which P_{Bk} calculated from Eq. (2) is compared to the measured indenter load, $P_{Bk,exper}$ (compare columns 9 and 10 in Table S2 [31]) at the time of ripplocation nucleation. Figure 2(b) compares the two graphically. The agreement has to be considered excellent since the problem solved is that of a column, while experimentally we tested plates. Furthermore, in the theory, we assume the indented layers are fused together, when in fact they are not. These calculations are thus consistent with our conjecture that buckling is the operative mechanism.

A. Fully reversible nested loops

Before proceeding further, it is important to establish the relationship between the energy dissipated per unit volume per cycle, W_d—given by the area enclosed by the fully reversible loops—and the strain associated with these loops. As W_d is clearly related to the formation of the RBs (Figs. S6–S8 of the SM [31]), we label that strain ε_{RB}. Note that since the reversible loops were obtained on unloading, ε_{RB} and the stresses are calculated assuming the origin is at the point of maximum stress, viz., point A in Figs. 4(a) and 4(b). For example, in Fig. 4(a), ε_{RB} and σ_{max} for the fifth loop are given by horizontal and vertical arrows, respectively. Under these conditions, the following relationship is valid [37]:

$$W_d = 2\tau_{RB}\gamma_{RB} \approx (1+\nu)\,\sigma_{RB}\varepsilon_{RB}, \tag{3}$$

where τ_{RB} and σ_{RB} are the shear and normal stresses needed to nucleate and move the RBs. It follows that τ_{RB} can be considered a critical resolved shear stress for RBs. γ_{RB} and ε_{RB} are the applied shear and normal strains; ν is Poisson's ratio assumed to be 0.3. The factor of 2 accounts for energy dissipated during loading and unloading. If we further assume Coulombic friction, then $P_S = \mu P_N$, where μ is the friction coefficient between the layers, and P_N and P_S are the loads acting normal and parallel to the layers, respectively.

When W_d is plotted vs ε_{RB} for the cards and steel sheets [Fig. 4(d)], the results fall into two regimes. For the cards (lower right), W_d is low and increases monotonically with increasing $P_{N,0}$. Least-squares fits of these results with, in all cases, $R^2 > 0.95$ yield slopes of 16.0, 18.1, and 22.9 MPa for $P_{N,0}$ of 400, 1200, and 2400 N, respectively. It follows from Eq. (3), assuming ν to be 0.3, that the respective σ_{RB} values are 12.3, 13.9, and 17.6 MPa.

Least-squares fits of the results with, in all cases, $R^2 > 0.96$, labeled steel in Fig. 4(d), resulted in slopes of 71.2, 71.2, and 72.4 MPa for $P_{N,0}$ of 400, 1200, and 2400 N, respectively. Again, making use of Eq. (3), $\sigma_{RB} \approx 55$ MPa. When the sheets were lubricated, at 51.5 MPa, the slope was significantly lower and the corresponding σ_{RB} value is ≈39.6 MPa. It follows, not surprisingly, that W_d in the presence of a solid lubricant is 75% the value in its absence. Coincidentally or not, the ratio of μ's with (0.12) and without (0.2) lubrication is 0.6 (see Table S1 in the SM and related discussion [31] for details of measurements of μ).

Note that W_d is essentially a product of μ and P_N. Since the RBs in the cards nucleate at significantly lower stresses than the steel sheets (see Table S2 of the SM [31]), it is not surprising that the σ_{RB}'s for the former are lower than the latter, despite the fact that their μ's—0.25 for the cards and 0.2 for the steel (see Table S1)—are comparable.

B. RBs nucleation stresses

The results shown in Figs. 4(a)–4(c) make it amply clear that the RB nucleation stresses not only depend on $P_{N,0}$, but as importantly on μ between the layers. For example, for the same $P_{N,0}$, the solid lubricant reduced the RB nucleation stresses from ≈220 to ≈150 MPa [compare red and black results in Fig. 4(b)].

Lastly, in this section, when the P_{Bk} values calculated from Eq. (2) and the experimentally measured buckling loads are compared [Fig. 2(b)], it is reasonable to conclude that despite its simplicity, our model captures the physics of what is occurring.

C. Molecular dynamics modeling of graphite

To further make the case that confined buckling is the operative mechanism and to convincingly show that this mechanism is operative over multiple orders of lengths scales, we use MD simulations on graphite—at 10 K—to show that most of the observations made herein also occur at the atomic level. We chose graphite because (i) the potentials are well known and proven, (ii) graphite is known to form kink bands—that have been ascribed to BDs—when compressed [30,38], and (iii) the weak interlayer bonds in graphite are a good model for the experiments we carried out. In our experiments, especially at low confining pressures, there is a sizable amount of "empty" space between the layers that is easily compressible when the RBs are nucleated. Said otherwise, both graphite and our indented layers are, at least initially, easily compressible along z, which, as discussed below, is critical to RB nucleation.

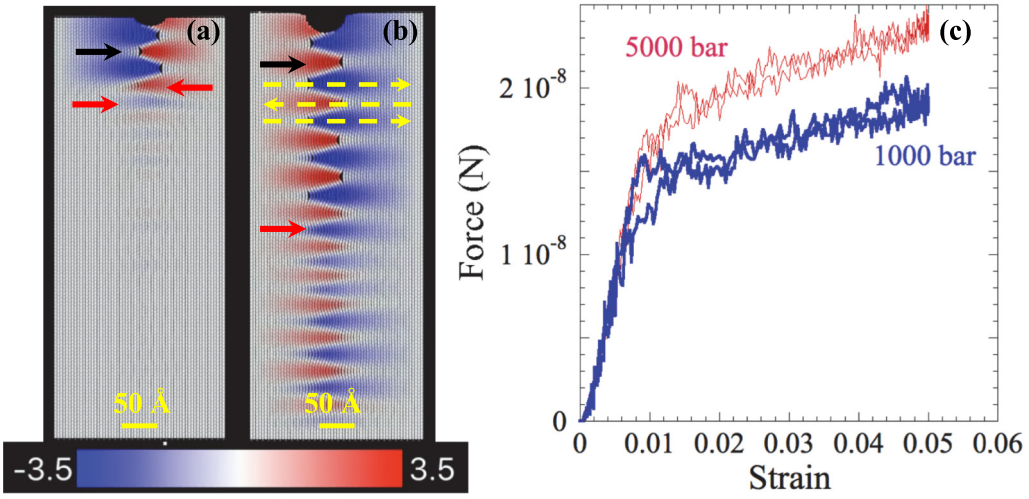

FIG. 5. MD modeling of graphite. Still frames taken from a MD simulation made when a 5-nm-diameter cylinder is loaded, edge-on, into 60 graphite layers—$P_{N,0} = 100$ bar—at (a) $½h_{max}$ and (b) h_{max} of 2.5 nm. (c) Nanoindentation force-strain results for two $P_{N,0}$ values, showing the initial linear elastic response followed by the formation of spontaneously and fully reversible loops. Color scale in (a) quantifies atomic motion along the z axis, in Å, to the right (blue) or left (red). Dashed yellow lines in (b) denote RBs of opposite signs. Red arrows point to regions where the deformation is accommodated without delamination; black arrows point to delaminations.

Movie S4 of the SM [31] shows what occurs when 60 graphite layers are loaded edge-on—with a 5-nm-diameter cylindrical indenter—in the same orientation as in our macro experiments. Snapshots, at roughly $½h_{max}$ and h_{max} of 2.5 nm, are shown in Figs. 5(a) and 5(b), respectively. The red and blue regions designate planes that moved to the left or right relative to their original position, respectively. In Figs. 5(a) and 5(b), $P_{N,0}$ was 100 bar. Figures S9a and S9b of the SM [31] show snapshots at h_{max} of 2.5 nm for $P_{N,0}$ of 0 and 1000 bar. Figure 4(f) plots P_N as a function of h and $P_{N,0}$.

From these results, the following is clear: (i) RBs nucleate at the top, near the indenter, first [Fig. 5(a)], and then quite rapidly indeed propagate, in a wavelike manner, to the end of the sample. (ii) Here again, confined buckling is the operative mechanism. (iii) Based on this picture, we define RBs *as the locus that connects the points of highest curvature in each layer*, shown by the dotted yellow lines in Fig. 5(b). In our perfect model, they are parallel to the surface and alternate in sign. (iv) If the RBs amplitudes are not too large, the curvature is accommodated without delaminations [red arrows in Figs. 5(a) and 5(b)]. At higher amplitudes, delamination cracks [black arrows in Figs. 5(a) and 5(b)]—such as the ones observed throughout this work—nucleate. (v) When Figs. 4(f) and 4(e) are compared, it is obvious that at least qualitatively, the relationship between P_N for the cards and for graphite is similar despite the fact that one is at the centimeter scale and the other at the subnanometer scale.

Figure 5(c) plots P vs h as a function of cycling with a rate of 5 m/s. Here again, increasing $P_{N,0}$ increases the BR nucleation stress. From the movie in the SM [31] and Fig. 5(c), it is clear that the process is *fully and spontaneously reversible*. However, is contrast to the other stress-strain curves shown in Figs. 4(a)–4(c), in this case, W_d is quite small. Interestingly, when the loading rate was increased to 50 m/s, W_d increased substantially (see Fig. S9c of the SM [31]). At this time, it is neither clear why the rate has such a significant effect on W_d nor why W_d is so small at relatively slower loading rates.

These comments notwithstanding and based on the results obtained herein, the driving force for reversibility is crystal clear: it is the energy stored in the curvature of the crests/troughs of the RBs *and* the energy stored in the layers compressed along z by the RBs. Friction between the layers results in W_d. These observations are crucial in understanding RB formation: Upon RB nucleation, not only is the strain massively delocalized, but strong in-plane bonds are replaced by weaker out-of-plane bonds. That is the essence of deformation by ripplocations.

With this insight, the reason why increasing $P_{N,0}$ increases the nucleation stress is clear: Rendering the out-of-plane deformation more expensive retards nucleation. This result is not new, but is well established in the geologic literature. For example, Kronenberg, co-workers, and others have shown that the kinking or failure stresses of micaceous single crystals are a strong function of confinement [3–5,39]. The same is true of layered composites [15], sheets of paper [17], and others.

D. RB wavelengths

In his work on the folding and buckling of layered geologic formations, Biot [12] derived this remarkably simple expression for the wavelength λ of buckled confined thin sheets:

$$\frac{\lambda}{t} = 1.9\sqrt{n}. \tag{4}$$

Here, n is the number of folded layers and t is their thickness. Biot emphasized that the expression is only valid if sufficient lubrication is retained at the interfaces between the layers, a good assumption here given the weak bonding between graphene layers. Assuming t for graphite to be ½ its c-lattice parameter, viz., 0.338 nm, Fig. S9d of the SM plots λ/t vs $n^{0.5}$ [31]. The linearity of the curve and its passing through the origin implies that Eq. (4) is remarkably well adhered to, even

at the atomic scale. This is especially true and appears to be valid even for a single graphene sheet (point near origin in Fig. S9d [31] obtained by buckling a single layer [21]). For reasons that are not clear, the slope in our case is not 1.9, but 3.5. This discrepancy notwithstanding, here again our results appear to capture the essence of the buckling physics that was originally derived for layered, viscous, geologic formations. Note that in contrast to geologic formations, where there is no control on the systems observed, here the use of perfect graphite layers allows for a clean and unambiguous measurement of all variables in Eq. (4).

The situation for the macroscopic experiments is different since as discussed above in our model, we assume—and the results confirm—that the n layers act as one with a thickness of $T = nt$. In that case, n in Eq. (4) is 1, and λ/T should be a constant $\approx$1.9. Table S3 in the Supplemental Material summarizes our results [31]. A perusal of these results shows that the cards are more or less in accord with Eq. (4). The situation for the steel depends on the friction coefficients. As noted above, Biot emphasized that Eq. (4) was only valid if the layers were well lubricated, and so it follows that the fact that the λ/nt ratio for the lubricated steel sheets was significantly lower than the unlubricated ones is consistent with this idea. Why the values are as high as they are is not clear at this time and more work is needed to understand the range and limitations of Biot's expression.

Based on the totality of our results, the sequence of events is as follows: First, ripplocations nucleate *en masse*, self-assembling into RBs that are mobile and fully reversible. With increasing load, the amplitudes of the RBs increase and the radii of their crests decrease. This cannot occur indefinitely; at a critical strain, the RBs will transform to the ubiquitous KBs found when *most* layered solids are compressed to *failure* [1]. It is worth repeating that this deformation/failure mechanism is totally agnostic as to whether the deformed layers are crystalline or amorphous. As shown here, even metals will deform by this mechanism if their aspect ratios are amenable to confined buckling (e.g., Figs. S2 and S3 of the SM [31]).

Figure S10 of the SM shows a Cr_2AlC single crystal that was deformed at high temperatures with minimal constraints [31]. The inset in this same figure shows what occurs to graphite layers that are compressed with *no* side constraints (i.e., allowing the layers to move freely in the z direction). Clearly the very convoluted structures obtained experimentally are readily generated in our MD models. This is important because it shows, once again, that our atomic level model is capable of producing features seen at the centimeter level. The similarity should persuade even the most hardened opposition as to the validity of the ideas promulgated here. This is not unique to the MAX phases. For example, Suematsu *et al.* [40] compressed SiC single crystals at 1500 °C and observed many of the features seen in Fig. S10. Along the same lines, and while this work deals with 2D systems, there is little doubt that these ideas also apply to one dimensional systems such as fibers, nanobrushes, etc., and should also apply to some polymers. In short any system in which the aspect ratios favor buckling.

It is important to note that the relationship between a single ripplocation and a RB is the same as that between a single-edge basal dislocation and a low-angle grain boundary. In the extreme case wherein an edge basal dislocation nucleates at every lattice plane, the boundary is indistinguishable from a $11\bar{2}1$ twin boundary (see Fig. S11 of the SM [31]) [41]. This is important because some have invoked the existence of KBs as evidence for the existence of BDs in layered solids.

The research on the deformation of layered systems in general has been on their failure [1]. In this work, we show that there is an important, nonlinear elastic regime that *precedes* failure that has, as far as we are aware, been almost totally neglected. The case can be made, however, that understanding this regime is *crucial and fundamental for understanding all others*.

In conclusions, layered solids—at all length scales—deform by confined buckling. The buckling nucleates RBs that rapidly propagate, wavelike, into the bulk. Before permanent and irreversible KBs form, a regime exists where RBs, that are, by definition, fully and spontaneously reversible, form. The driving force for this reversibility is the elastic energy stored in the crests of the ripplocations *and* that stored in the compression of layers adjacent to the RBs. The movement of the layers relative to each other is responsible for the energy that is dissipated. Nature's solution to the impossibility of c-axis strain in layered solids is remarkably simple and universal: buckling. By doing so, "expensive" in-plane strain is converted to much "cheaper" out-of-plane strain and delocalized over distances that are much longer than the size of the indenter. The fact that one can learn something about an earthquake from studying the deformation of graphite, or vice versa, is quite astonishing and remarkable indeed.

ACKNOWLEDGMENTS

This work was funded by the CMMI division of the National Science Foundation under Grant No. 1728041. We would like to thank Prof. R. Doherty of Drexel University for his invaluable insight and Prof. T. Ouisse at the Institut Polytechnique de Grenoble, Grenoble, France, for the micrograph shown in Fig. S10 of the Supplemental Material [31].

[1] C. J. Budd, R. Butler, and G. W. Hunt (eds.), Philos. Trans. R. Soc. A **370**, 1723 (2012).

[2] M. W. Barsoum, *MAX Phases: Properties of Machinable Carbides and Nitrides* (Wiley VCH GmbH, Weinheim, 2013).

[3] R. Christoffersen and A. K. Kronenberg, J. Struct. Geol. **15**, 1077 (1993).

[4] A. Kronenberg, S. Kirby, and J. Pinkston, J. Geophys. Res. **95**, 19257 (1990).

[5] V. M. Mares and A. K. Kronenberg, J. Struct. Geol. **15**, 1061 (1993).

[6] B. T. Kelly, *Physics of Graphite* (Applied Science, London, 1981).

[7] A. Meike, Am. Mineralogist **74**, 780 (1989).
[8] M. W. Barsoum, T. Zhen, A. Zhou, S. Basu, and S. R. Kalidindi, Phys. Rev. B. **71**, 134101 (2005).
[9] J. B. Hess and C. S. Barrett, Metals Trans. **185**, 599 (1949).
[10] F. C. Frank and A. N. Stroh, Proc. Phys. Soc. **65**, 811 (1952).
[11] P. J. Hudleston and S. H. Treagus, J. Struct. Geol. **32**, 2042 (2010).
[12] M. A. Biot, Geol. Soc. Amer. Bull. **76**, 833 (1965).
[13] B. Budiansky, N. A. Fleck, and J. C. Amazigo, J. Mech. Phys. Solids **46**, 1637 (1998).
[14] S. Kriakides and A. E. Ruff, J. Comput. Mater. **31**, 2000 (1997).
[15] S. Narayanan and L. S. Schadler, Composites Sci. Technol. **59**, 2201 (1999).
[16] S. R. Reid and C. Peng, Int. J. Impact Eng. **19**, 531 (1997).
[17] G. Mullineux, B. J. Hicks, and C. Berry, Philos. Trans. R. Soc. A **370**, 1925 (2012).
[18] K. Kendall, Nature (London) **261**, 35 (1976).
[19] A. Schallamach, Wear **17**, 301 (1971).
[20] J. Griggs, A. Lang, J. Gruber, G. J. Tucker, M. Taheri, and M. W. Barsoum, Acta Mater. **131**141 (2017).
[21] J. Gruber, A. Lang, J. Griggs, M. Taheri, G. J. Tucker, and M. W. Barsoum, Sci. Rep. **6**, 33451 (2016).
[22] D. Frieberg, M. W. Barsoum, and G. J. Tucker, Phys. Rev. Materials **2**, 053602 (2018).
[23] A. Kushima, X. Qian, P. Zhao, S. Zhang, and J. Li, Nano Lett. **15**, 1302 (2015).
[24] M. W. Barsoum and G. J. Tucker, Script. Mater. **139**, 166 (2017).
[25] M. W. Barsoum, A. Murugaiah, S. R. Kalidindi, and T. Zhen, Phys. Rev. Lett. **92**, 255508 (2004).
[26] N. G. Jones, C. Humphrey, L. D. Connor, O. Wilhelmsson, L. Hultman, H. J. Stone, F. Giuliani, and W. J. Clegg, Acta Mater **69**, 149 (2014).
[27] A. G. Zhou and M. W. Barsoum, J. Alloys Compds. **498**, 62 (2010).
[28] M. W. Barsoum, T. Zhen, S. R. Kalidindi, M. Radovic, and A. Murugahiah, Nat. Mater. **2**, 107 (2003).
[29] S. Basu, A. Zhou, and M. W. Barsoum, J. Struct. Geol. **31**, 791 (2009).
[30] M. W. Barsoum, A. Murugaiah, S. R. Kalidindi, and Y. Gogotsi, Carbon **42**, 1435 (2004).
[31] See Supplemental Material at http://link.aps.org/supplemental/10.1103/PhysRevMaterials.3.013602 for Materials and Methods, Movies S1 to S4, and Figs. S1 to S12.
[32] C. M. Wang, C. Y. Wang, and J. N. Reddy, *Exact Solutions for Buckling of Structural Members* (CRC, Boca Raton, FL, 2004).
[33] S. J. Stuart, A. B. Tutein, and J. A. Harrison, J. Chem. Phys. **112**, 6472 (2000).
[34] S. Plimpton, J. Comp. Phys. **117**, 1 (1995).
[35] A. G. Zhou, M. W. Barsoum, S. Basu, S. R. Kalidindi, and T. El-Raghy, Acta Mater. **54**, 1631 (2006).
[36] R. Benitez, W. Hao, H. Gao, M. O'Neil, G. Proust, and M. Radovic, Acta Mater. **105**, 294 (2016).
[37] J. M. Roberts and N. Brown, Trans. AIME **218**, 454 (1960).
[38] E. J. Freise and A. Kelly, Proc. Phys. Soc. A **264**, 269 (1961).
[39] M. S. Patterson and L. E. Weiss, Geol. Soc. Amer. Bull. **77**, 343 (1996).
[40] H. Suematsu, T. Suzuki, T. Iseki, and T. Mori, J. Amer. Cer. Soc. **74**, 173 (1991).
[41] N. J. Lane, S. I. Simak, A. S. Mikhaylushkin, I. A. Abrikosovv, L. Hultman, and M. W. Barsoum, Phys. Rev. B **84**, 184101 (2011).